Development of a Maxwell X-57 High Lift Motor Reference Design

Dustin L. Hall*, Jeffrey C. Chin†, Aaron D. Anderson‡, Jerald T. Thompson§, Andrew D. Smith¶, Ryan D. Edwards‖, and Kirsten P. Duffy**
NASA Glenn Research Center, Cleveland, OH, 44135, U.S.A.

NASA's all-electric X-57 airplane will utilize 14 electric motors, of which 12 are exclusively for lift augmentation during takeoff and landing. This report covers the design and development process taken to create an open reference model representative of the high lift augmenting motors. A combined worst case scenario was used as the design point, which represents the simultaneously occurring worst case aspects of thermal, static stress, electromagnetic, and rotor dynamic conditions. This work highlights the tightly coupled nature of aerospace electric motor design. The cooling method uses forced convection cooling on the nacelle skin; no internal air flow is permitted. The stator outer diameter limit of 156.45 mm greatly impacts the degree of coupling between the electromagnetic design with the thermal analysis. The permanent magnet synchronous motor developed here operates between 385 V and 538 V, at a peak current of 50 A. Detailed electromagnetic, thermal, static load, and rotordynamic analysis was completed for this electric motor; all of which are required for a full design. The rotordynamic analysis took into consideration the motor housing which is designed specifically for this motor. The final electric motor has a mass of 2.34 kg resulting in a positive mass margin of 16.8 %, produces 24 Nm of torque with a specific power of 5.64 kW/kg, and has an efficiency of 96.6% at the combined worst case design point.

I. Nomenclature

A_{cw}	cross section area of a copper wire (mm^2)	k_e	epoxy thermal conductivity ($\frac{W}{m^\circ C}$)
A_s	area of slot (mm^2)	K_{eddy}	eddy current loss coefficient
α	hysteresis loss empirical constant	K_h	hysteresis loss coefficient
B	flux density (T)	K_{radial}	radial thermal conductivity ($\frac{W}{m^\circ C}$)
Cu_f	copper fill factor (%)	N_m	number of magnets poles
f	fundamental frequency (Hz)	N_s	number of stator slots
$h_{c,m}$	convection coefficient ($\frac{W}{m^\circ C}$)	N	number of wire turns in coil
i	current (A)	T	torque (Nm)
J	current density (A/mm^2)	W_{fe}	iron losses ($\frac{W}{kg}$)
K_{axial}	axial thermal conductivity ($\frac{W}{m^\circ C}$)	V_{DC}	voltage, direct current
k_c	copper thermal conductivity ($\frac{W}{m^\circ C}$)		

*Propulsion Systems Analysis Branch, dustin.l.hall@nasa.gov, AIAA Member
†Propulsion Systems Analysis Branch, jeffrey.c.chin@nasa.gov, AIAA Member.
‡Diagnostics and Electromagnetics Branch, aaron.d.anderson-1@nasa.gov.
§Structural Mechanics Branch, jerald.t.thompson@nasa.gov
¶Thermal Fluid Systems Branch, andrew.d.smith-1@nasa.gov AIAA Member.
‖Thermal Fluid Systems Branch, ryan.d.edwards@nasa.gov
**Rotating Systems Branch, kirsten.p.duffy@nasa.gov, AIAA Member

II. Introduction

Fig. 1 Rendering of the X-57, depicting the inboard high lift assembly and the larger cruise motors located on the wing tips

The X-57, NASA's first all-electric X-plane, is being designed to help determine the added benefits of a distributed electric propulsion system, applied to an array of small motors used to generate lift. The distributed electric propulsion system consists of 12 electric high lift motors (HLM) attached at the leading edge of a composite, high aspect ratio wing, along with two larger cruise motors attached at the wing tips, which can be seen in Fig 1. All 12 HLM's on the X-57 are 13.7 kW permanent magnet synchronous motors (PMSM), designed to be used only during takeoff and landing and during a maneuver that will simulate a climb at a maximum altitude of 10,000 feet. The X-57 is propelled by the wing-tip cruise motors during cruise, with the high lift system turned off to decrease drag. Goals for the X-57 is a 500% decrease in energy during the high-speed cruise, with zero carbon emissions and a reduction in noise. Fig 2 shows the high lift system and depicts the location of the motor within the housing.

This report details the design process, required analysis, and performance of the HLM. Aggressively minimizing mass leads to thin design margins, requiring detailed thermal, electromagnetic, and rotordynamic analyses. When thermal and electromagnetic properties are pushed to operational limits to decrease mass, while simultaneously minimizing losses, all aspects of the design become coupled to an even higher degree. The stator outer diameter limit of 156.45 mm, and the mass limit of 2.77 kg provided considerable constraints to all aspects of the design. The geometry, electromagnetic performance, and thermal behavior are all highly coupled due to the relatively small outer diameter, lack of cooling, and the power requirements. The final design then went through rotordynamic analysis, which helped to design the motor housing and interior support of the motor.

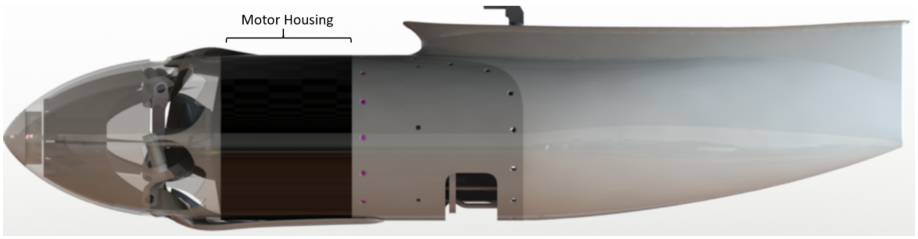

Fig. 2 High lift nacelle showing location of the high lift motor

A. In-house Design Motivation

Although NASA collaborates extensively with external businesses on many aspects of the vehicle design and fabrication, it was considered worthwhile to invest time in a reference design HLM for numerous reasons. NASA Glenn Research Center (GRC) drafted the initial specification for both the motor and controller, and generated the inverter design which will be used for the HLM. GRC also has both, motor design heritage as well as many of the required testing and validation capabilities in-house and readily available. GRC is also responsible for thermal analysis across the entire high lift nacelle which includes the heatsink for the high power electronics, aft of the HLM, and can incorporate the design directly into the vehicle Mission Planning Tool [1]. Internal NASA designs allow for a clear path forward for technology transfer not only for the current project, but into future projects as well with deeper integration and

open-source references. The prime contractor, ESAero, is ultimately responsible for procuring the actual motor and hardware for the final design.

B. Requirements

NASA has developed a list of requirements for the HLM through system and sub-system level studies. These requirements push the motor to a very high power density, and the tradeoff between mass and thermal becomes a highly coupled issue. The following list describes high level requirements which must be met by the HLM [2].

1) Performance Specifications
   - Provide 24 Nm of torque between 2000 and 5450 RPM and 22 Nm of torque at 5460 RPM.
   - Have a minimum efficiency of 93% at 460 V_{DC} bus voltage at 10.5 kW and 5460 RPM.
2) Electrical Requirements
   - The motor operating voltage shall be between 385 V_{DC} and 538 V_{DC}.
   - The motor windings shall sustain a non-operating voltage of 1200 V_{DC} between the motor windings and motor housing without degradation of motor performance or damage to the motor.
   - The motor shall have 3 phases.
   - The motor shall be compatible with a maximum peak phase current amplitude of 50 amps at the fundamental frequency.
   - The motor's minimum phase inductance shall be 75 μH
   - The motor bonding material (epoxy, etc) shall be rated at 220 $^{\circ}C$ or higher
3) Physical Requirements
   - The high-lift motor's diameter, including housing, shall not exceed 6.36 inches (161.5 mm)
   - The high-lift motor's length (depth) shall not exceed 2.6 inches (66.4 mm)
   - The high-lift motor shall be less than six pounds.

Requirements for electric motors must be developed in conjunction with specific design points and operational parameters. Two portions of the flight profile have been identified which give rise to the worst cases with regards to thermal, rotor dynamic, structural, and electromagnetic aspects. First is the pre-flight run-up which tests the electric motors while the aircraft is static, at 4,400 RPM for 30 seconds. The run-up proves to be the worst case for thermal design, as the cooling is minimal and the input power is high. The next worst case scenario is the high lift assembly assisted climb at a maximum allowable altitude of 10,000 ft above sea level. This is the worst case for all other aspects; the static load, electromagnetic, and rotordynamic performance.

Figure 3 displays a plot of thrust with a linear torque schedule (left) and a plot of power with a linear torque schedule (right) in terms of velocity and altitude. The pink box represent the takeoff and landing envelope, while the black box represents the cruise and simulated climb envelope. The left boundary condition of both envelopes represent the worst case scenario in that particular phase of flight. The HLM is designed using a combined worst case scenario using data from the top left section of the cruise and simulated takeoff envelope, and the run-up condition which is not explicitly listed in Fig 3.

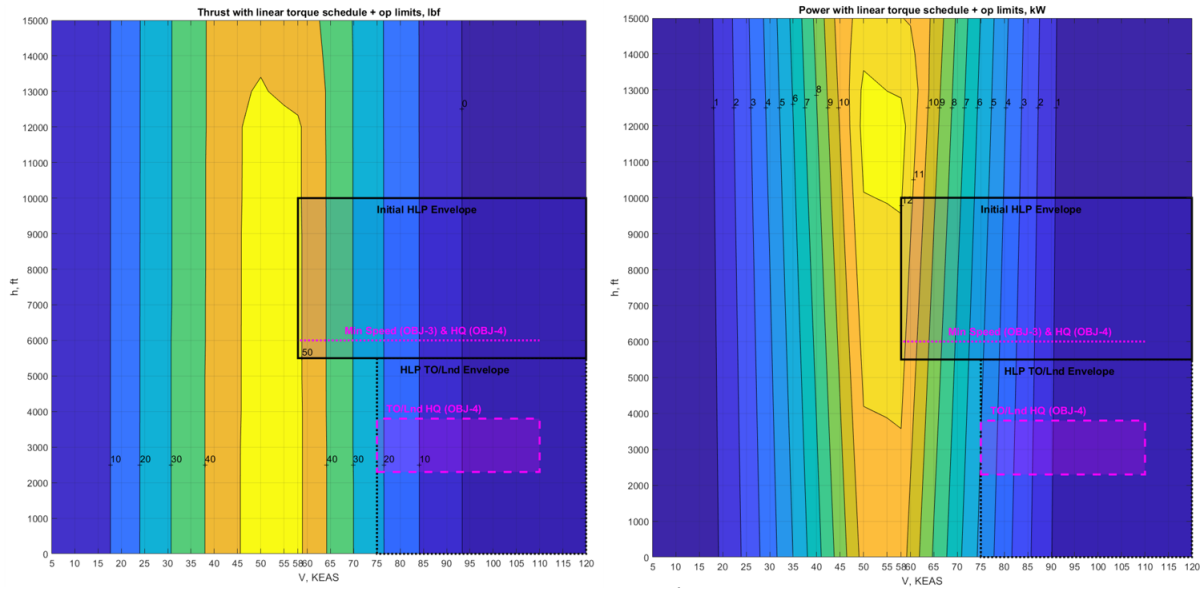

Fig. 3 Scheduled high lift assembly thrust (left) and power (right) with an overlaid takeoff and landing envelope (pink) and cruise/simulated climb envelope (black)

III. Overall Design Process

The HLM design is a highly coupled problem involving multiple disciplines, each requiring input data developed from separate analysis. Figure 4 shows the high level design and iteration process taken to develop the HLM. The yellow ovals represent the primary design steps, the boxes to the right of each step are outputs, while boxes to the left are values fed back to upstream steps, signifying a required convergence loop coupling. Values with an asterisk next to them represent a re-calculated value from the previous design step. Fig 4 is formatted to represent the layout of the remainder of this report, each step has a reference to the appropriate section in bold lettering.

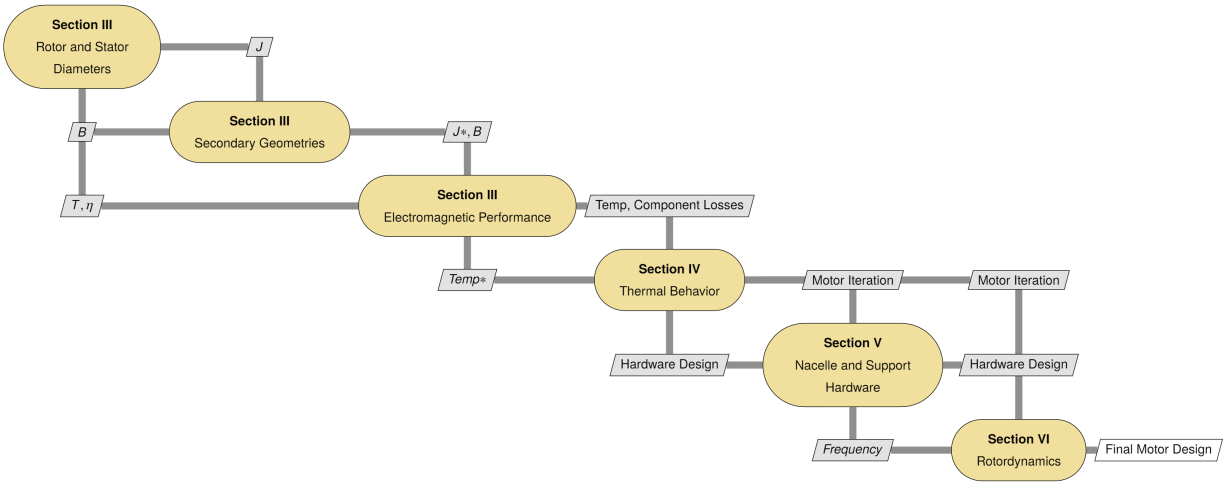

Fig. 4 A high level diagram depicting the workflow of the design process. The asterisk represents re-calculated values from the original input/output values.

Current density (A/mm^2), shown in Equation 1, is used as a primary parameter to size the motor from a thermal aspect by limiting losses generated in the windings of the slot area. As the rotor outer diameter increases, the stator inner diameter must proportionately increase as well, shrinking the slot area. Decreasing the slot area while holding the

current and stator outer diameter constant causes the current density to increase, increasing winding losses. Figure 5 depicts the geometric considerations taken into account during the design process.

$$J = 2Ni\sqrt{2} * \frac{N_s * A_s * 10^5}{f} \tag{1}$$

Where J is the current density, A_s is the annulus area where the slots are located, 10^5 is a unit conversion constant, and f is the copper fill factor.

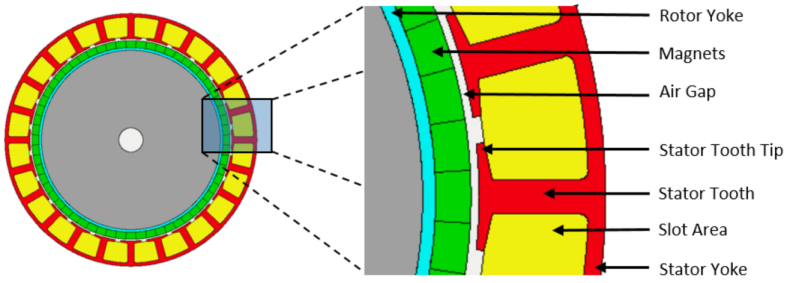

Fig. 5 Geometric parameters taken into consideration in each step of the design process. The light blue represents the rotor iron, green represents the magnets, red represents the stator iron, and the yellow represents the slot area where the windings are located.

Once the stator and rotor diameters are defined and the current density reaches approximately 11 A/mm^2, the design progressed to calculating the secondary geometries. The secondary geometries are referred to as the rotor yoke thickness, stator tooth tip, stator tooth, and the stator yoke thickness and are minimized as a function of flux density. After a successful electromagnetic design i.e. torque and efficiency reached required values, component losses were used for a steady state thermal analysis. It is important to make initial boundary conditions for temperature of some key components such as the ambient air, windings, stator, rotor, and magnets up front as these initial temperatures directly affects the performance and losses. After a design was closed electromagnetically and thermally, a nacelle structure was built around it, and then analyzed for static loading and rotordynamic performance.

IV. Electromagnetic Design

This section discusses the iterative design process taken to develop the HLM. This is a highly coupled problem with thermal management, rotordynamics, and static loading which have large impacts during the design process. Determining a proper design point was key in initial sizing for the motor, used here is the combined worst case scenario. After each iteration, re-sizing of the rotor and stator were often required based on the current density being too high causing an unacceptable level of losses, and flux density values not taking full advantage of the stator and rotor materials.

A. Stator and Rotor Design

As magnetic flux is generated, the Lorentz force is developed and is exerted between the coils and magnets. The magnetic flux passes through the air gap, into the stator where the tangential force produces torque. Using electrical steels with high flux density saturation points allows for the reduction of mass by allowing more flux to flow through a smaller area. Grain oriented electrical steel reduces hysteresis losses, while thin electrically isolated sheets, or laminations, reduce eddy current losses. The stator and rotor for the HLM will be constructed from Hiperco-50 using laminations with a 0.006 inch thickness.

One of the biggest benefits of using Hiperco-50 is the maximum flux density saturation point of 2.4 T. Figure 6 depicts the 2-D FEA results for the magnetic flux densities in the stator and rotor at a defined instant in time assuming a maximum peak current of 50 A. The average flux density between the stator teeth and the stator yoke is between 2.3 T and 2.4 T. Although the scale shows flux densities higher than 2.4 T in some areas, this is deemed to be a negligible area of over-saturation. Relevant Hiperco-50 material properties are listed in Table 1 for reference.

The rotor yoke thickness, stator yoke thickness, stator teeth width, and tooth tip thickness are all minimized to reduce weight by achieving a flux density of approximately 2.4 T, see Fig 5 for geometric references. The slot area is

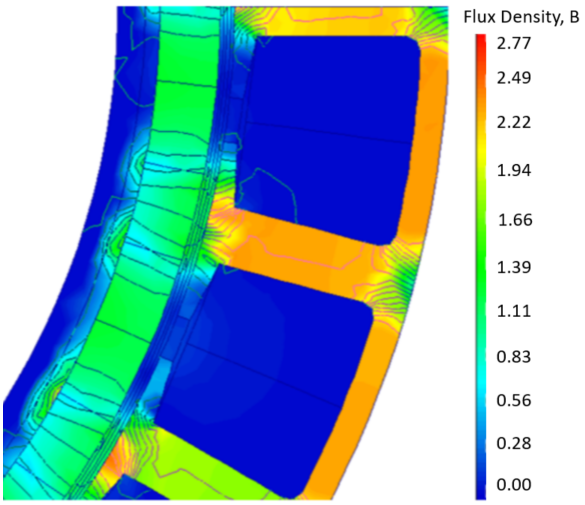

Fig. 6 2-D FEA flux density calculations for the rotor and stator back-irons

simultaneously minimized as a result of increasing the stator inner diameter until the current density of the windings reaches approximately 11 A/mm^2. Specifying a maximum allowable current density is a proxy to designing to an allowable level of losses in the windings, which reduces the number of iterations between electromagnetic and thermal analysis. Once the current density is reached, assuming the outer diameter of the motor is held constant and the slot/pole combination is fixed, a maximum allowable inner diameter for the stator can be determined.

The HLM stator and rotor are constructed from a stack of 0.006 inch Hiperco-50 laminations, each lamination cut using a laser. An electrically isolating material, C5 [3] is used to between each lamination to reduce development of eddy currents in the stator and rotor. Each lamination is annealed after being cut to relieve the mechanical stress at the boundaries developed under the heat of the laser. When the stator and rotor are constructed, the laminations are bonded with EB-548 epoxy and a spot weld is used to provide further integrity to the structure.The maximum operating temperature of the bonding agent EB-548 is $140°C$ per the manufacturers specifications. Although the temperature of the stator and/or rotor have the potential to reach higher temperatures, the maximum temperature plays a minimal role due to the additional weld and the fact that the stator will be dipped in epoxy (potted). For a plot of EB-548 performance versus temperature, please refer to Fig 21 in the appendix.

Common thicknesses for laminations are 0.014 inch and 0.006 inch, a study was done to determine losses between both thicknesses. Holding all other parameters constant, reducing the lamination thickness from 0.014 inches to 0.006 inches results in a substantial stator loss decrease from 286 W to 117.6 W respectively. Hysteresis and eddy current losses are calculated in Motor-CAD using a modified Steinmetz equation [4], which can be seen in Equation 2.

$$W_{fe} = \underbrace{(K_h f * B^{(\alpha * B)})}_{hysteresis} + \underbrace{(2\pi^2 * K_{eddy} f^2 B^2)}_{eddy} \tag{2}$$

Where W_{fe} is the iron losses (W/kg), K_h is the hysteresis loss coefficient, α is an empirical constant, and K_{eddy} is the eddy current loss coefficient. All variables listed above are defined by curve fitting core loss data from four loss curves at different frequencies for Hiperco-50, Motor-CAD automatically calculates these values during analyses. Finally, B is flux density (T), and f is the fundamental frequency (Hz). For the Hiperco-50 loss plots used to determine the iron losses using the modified Steinmetz equation, please see Fig 23 in the appendix.

B. Magnets

Several magnet options exist for this application, important characteristics to consider are the maximum operational temperature of the magnets, energy density, the remanence flux values, and cost. It was determined N48H magnets best fit this application with a maximum operating temperature of $120°C$. The maximum magnet temperature is highly sensitive to the design point of the motor, and is further complicated in this case due to no internal cooling. Other magnets considered for this application, and their properties [5], are listed in Table 2.

Table 1 Hiperco-50 material properties

Property	Units	Value
Physical Properties		
Density	kg/m^3	8120
Melting Point	$^\circ C$	940
Electrical Resistivity	$\mu\Omega cm$	40
Thermal Conductivity	$W/cm^\circ C$	29.8
Thermal Expansion ($25^\circ C$ - $500^\circ C$)	$ppm/^\circ C$	10.4
Specific Heat	$kJ/kg^\circ C$	0.42
Annealed Mechanical Properties		
Tensile Strength	MPa	814
Yield Strength	MPa	435
DC Magnetic Properties		
Saturation Induction	T	2.40
Maximum Permeability	H/m	12,000
Coercive Force	A/m	72

Table 2 Possible magnet choices available for the X-57 HLM application

Grade	Remanence (T)	Coercivity (KA/m)	Intrinsic Coercivity	Energy Density ($KJ/m3$)	Max Op Temp ($^\circ C$)
N48H	1.390	1046	1353	378	120
N50H	1.415	1066	1274	390	120
N48SH	1.390	995	1512	374	150

Studies done in Motor-CAD show that torque from a conventional North South (N-S) array compared to a Halbach array can increase from 22.7 Nm to 24 Nm respectively. To reduce eddy current losses, the magnets were axially laminated, Fig 7 shows the effects of increasing the number of magnet laminations has on the losses. All studies done here are at the previously defined combined worst case scenario. Eight lamination segments results in approximately 15 W of losses, or 3.5% of the magnitude of total losses. Increasing to nine segments increases cost, complexity, and possibly lead time for a negligible 0.49% decrease in percent total losses when compared to eight segments.

C. Slot to Pole Fraction and Winding Factor

The nature of having a different number of slots and poles introduces a parameter referred to as the winding factor and requires concentrated windings. Concentrated windings introduce a fractional slot pitch, which decreases efficiency and torque when compared to a distributed winding layout. The optimal winding layout is determined by describing the back EMF and winding factor through a set of Fourier series which assumes the back EMF changes only with phase offset [6]. Table 3 shows combinations of slots and poles considered for this project along with the winding factor. The grayed out boxes in the table represent an invalid slot/pole combination.

Magnetic noise must be considered when determining the slot pole combination. Calculating the radial magnetic noise, or radial forces attracting the rotor and stator together, produced for a slot/pole combinations aids in the determination of valid slot/pole combinations. This design uses 24 slots and 20 poles with a winding factor of 93.3%. It is possible to achieve a higher winding factor for 21 slots and 20 poles, but the unbalanced magnetic pull angle is an unacceptable 154 degrees, creating an unbalanced force of 169 N. Whereas the 24 slot, 20 pole design results in a uniform 179 degree of unbalanced magnetic pull angle, resulting in a negligible 1.7 N. Libert and Soulard suggests avoiding any slot pole combinations giving winding layouts that are non symmetrical [7] causing uneven radial forces. Equations 3 shows number of slots to avoid, while Equation 4 shows the number of poles to avoid.

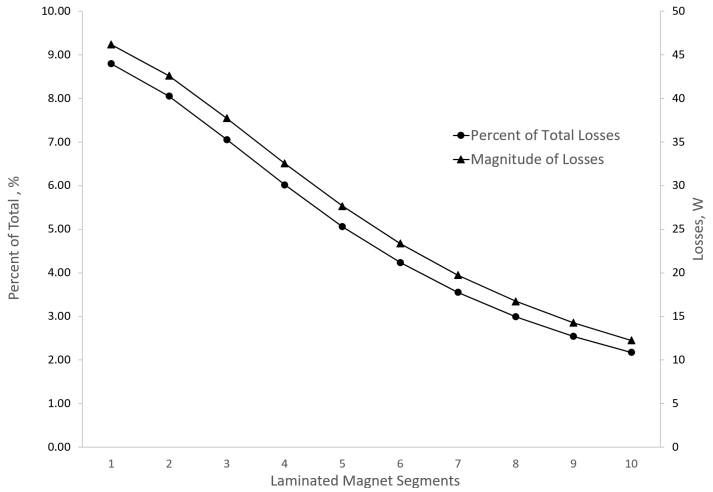

Fig. 7 How magnet losses decrease as the number of magnet laminations increase. The magnitude of losses (triangle data points) correlates to the right axis and the percentage of magnet losses to total losses (circle data points) correlates to the left axis.

Table 3 Winding factors based on slot/pole combinations

Slots\Poles	12	14	16	18	20	22
12		93.3	86.6		50	25
15		95.1	95.1		86.6	71.1
18	86.6	90.2	94.5		94.5	90.2
21		86.6	89		95.3	95.3
24		76	86.6		93.3	94.9
27	94.5	69.5	76.6	86.6	87.7	91.5

$$N_s = 9 + 6k \tag{3}$$

Where N_s represents the number of slots and k is any positive integer.

$$N_m = N_s \pm 1 \tag{4}$$

Where N_m is the number of magnetic poles. The effect of using a non-recommended slot/pole combination described by Equation 4 can be seen in the high unbalanced radial forces acting on the rotor.

D. Coils

It is advantageous to pack the maximum amount of copper inside each slot area. Once the optimal number of turns is found, increasing the number of strands-in-hand for the litz wire will decrease the current density, and have the same effect on the wire losses, ultimately decreasing mass. The relationship between the current density, copper losses, and mass here again highlight the tightly coupled nature of this design. The coil fill factor, which can be seen in Equation 5, controls the amount of copper per slot area. The coil fill factor is a primary design consideration, and was held to approximately 60% for all design studies. Though 60% is an optimistic value for low voltage motors [8], it is an achievable goal with proper planning and practice.

$$K_{cw} = \frac{NA_{cw}}{A_s} \tag{5}$$

Where N is the number of turns, A_{cw} is the cross sectional area of the covered wire, and A_s is the cross sectional area of the slot. Care must be taken when using litz wire versus single wire for coil windings, Equation 5 must account

for the multiple wires in hand. The choice of litz wire is an important design consideration that must be included in the analysis, as it effects the fill factor, achievable number of turns per coil, current density, and wire resistance losses.

The dielectric strength and insulation resistance is very important for safety reasons, a wire-stator short would be a catastrophic failure. According to IEEE 95-2002 [9] the motor insulation should be rated to at least twice the maximum operating voltage plus 1000 V, according to these guidelines, HLM insulation should be rated to at least 2,076 V_{DC}. A 0.005 inch thick Nomex 410 layer is used as an insulator between the coils and the stator to prevent a voltage arc and/or leakage current from flowing to the stator. According to the Nomex 410 manufacturer, the dielectric strength of the 0.005 inch Nomex 410 is 715 V/mil or 3,575 V_{DC}, much higher than the recommended voltage. For property materials of Nomex 410, reference Fig 22 in the appendix.

The temperature of the wire insulation is an additional factor that must be considered. Each strand of litz wire is coated with a single layer of polyimide (MW16-C) insulation, having a maximum operating temperature of 240 $°C$ [10]. If at any point the stator or the coils reach this temperature, the insulation of the wires will break down and cause wire-wire shorts. Primary coil design variables used to control the motor performance are listed in Table 4.

Table 4 Coil configuration

Characteristic	Value
Copper fill factor	56.18%
Coil fill factor	58.41%
Litz wire bundle type	1
Litz wire layout	28 AWG, 48 in hand
Number of windings	12
Wire Insulation	Polyimide MW-16C
Slot insulation	Nomex-410
Number of slots	24
Winding factor	93.1%
Connection type	Star (Wye)
Worst case current density	10.7 A/mm^2

E. Electromagnetic Performance

Electromagnetic performance refers to the torque versus speed behavior, efficiency at the specified operating point, and component losses. Each topic discussed in this section is highly dependent on the losses, coupled with the mass, and thermal behavior. Component losses must be generated from the electromagnetic model assuming accurate temperatures up front which requires multiple iterations between electromagnetic and thermal analysis. The relationship between electromagnetic performance, and thermal behavior can be referenced in Fig 4.

1. Component Losses

Component level loss estimates are required for accurate thermal analysis, which will be discussed in more detail later in the report. Choosing the combined worst case design point pushes the maximum current through the motor, which generates the maximum losses. The majority of losses originate from the coils and the stator, if this is not the case a re-design will be necessary due to the specific cooling method used here. It is important to note again that laminated magnets are used in a Halbach array, and both back-irons are 0.006 inch laminated Hiperco-50 electrical steel. The nature of obtaining losses is highly coupled with the thermal performance of the motor and requires multiple iterations between thermal analysis and electromagnetic loss calculations until the assumed electromagnetic temperatures converge with the thermal analysis temperatures. Table 5 shows the converged temperatures and the final magnitude of component losses.

Despite having a lamination thickness of 0.006 inches, the eddy currents still dominate the stator losses. Eddy currents for the stator are 74.4 W, while the hysteresis losses are only 43.4 W.

Table 5 Final converged values for component temperatures and loss magnitudes

Component	Temperature (°C)	Total Losses (W)
Stator	128	117.6
Windings	129	253.8
Magnets	90	15.0
Rotor	78	3.85

2. Torque Versus Speed

The torque-speed curve is highly sensitive to the current, voltage, efficiency, and number of turns in the slot. The design point determines the current and voltage, and choosing to use the combined worst case design point ensures the torque will never fall below the required levels. The HLM is required to produce 24 Nm of torque from 2000 RPM to 5400 RPM. Figure 8 represents the torque-speed curve at the combined worst case scenario, with the supply voltage at 385 V_{DC} and 50 A_{peak}.

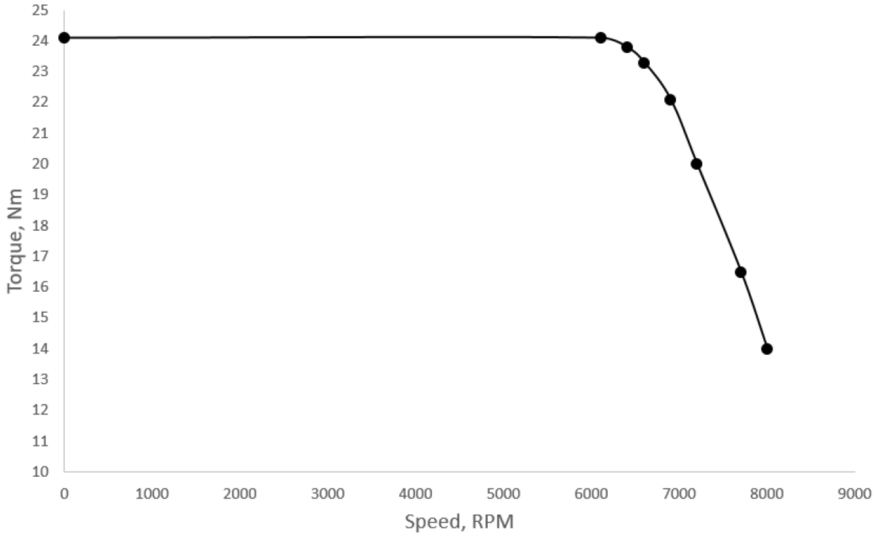

Fig. 8 Torque vs. speed curve for the HLM at the combined worst case scenario

The torque-speed curve can be seen in Fig 8, which accounts for all losses and temperatures listed in Table 5. Temperature increases in the magnets causes the remanence flux to decrease from the nominal 1.39 T at 20 $°C$, to 1.273 T at 90 $°C$. Despite the temperature increase, the torque requirement continues to be met, and begins to drop off at approximately 6,100 RPM. The torque drop at high RPM is due to the voltage available to the motor. Figure 8 shows that the motor will still be able to perform should the battery voltage drop below the minimum voltage of 385 V_{DC}.

3. Efficiency

The efficiency is plotted using a design point stated in the X-57 requirements document, 4400 RPM, 22 Nm of torque, at 460 V_{DC}. Figure 9 plots the efficiency as the motor moves through the RPM and torque ranges. The efficiency requirement at this operating point is 93%, but from Fig 9 it can be seen the motor will operate well above that at 96.61%. This is assuming current is sampled from 5 A_{peak} to 50 A_{peak}, an additional 50 W of mechanical losses are assumed from the bearings.

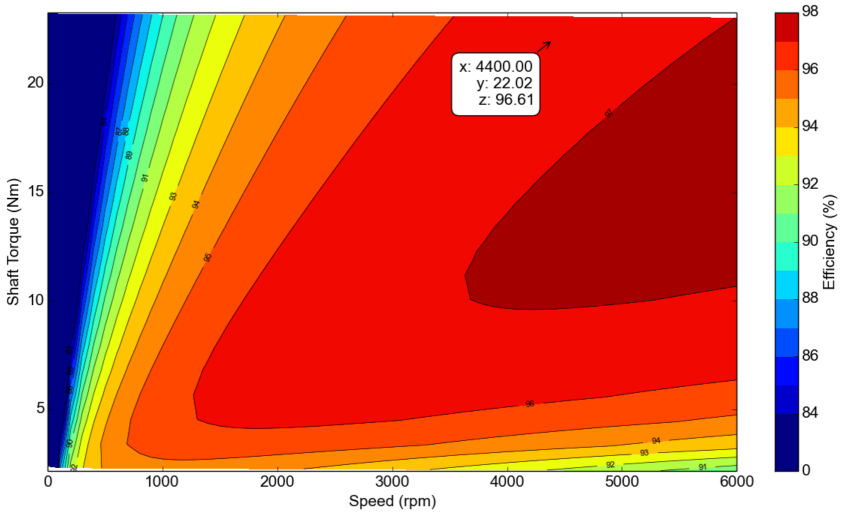

Fig. 9 Efficiency plot at the design point of 4,400 RPM, 22.89 Nm of torque, at 460 V_{DC}. The white box in the figure shows explicitly the RPM (x), torque (y), and the efficiency (z).

V. Thermal Analysis

Due to the tightly coupled nature of temperature and performance, component losses are required up front, and used in multiple thermal breakout models. Estimation of the heat transfer coefficients and near-wall conditions for the nacelle skin, and internal surface was completed using a series of CFD models. Convection heat transfer characterization was performed using ANSYS CFX, while detailed assembly heat transfer modeling was conducted using a coupled COMSOL model. A steady state thermal model was developed concurrently with the motor geometry and electromagnetic performance. Closing the HLM thermal design requires good characterization of the following:

1) Forced convection boundary conditions for the nacelle skin
2) Location and magnitude of significant volumetric heat fluxes (component electrical losses)
3) Effective heat transport properties of composite materials

A. Nacelle Skin Cooling and Internal Heat Transfer Characterization

A fully transient model was developed in ANSYS using an immersed rotor method to understand the interaction between the propeller and the near-wall air flow. Inlet boundary conditions simulate the static run-up conditions at 60 $^{\circ}C$ ambient temperature, corresponding to the combined worst case scenario. Figure 10 displays the model developed in ANSYS. The mesh size used to developed this model has a maximum size of 0.05 inches, and is solved using the universal Reynolds-averaged Navier–Stokes method.

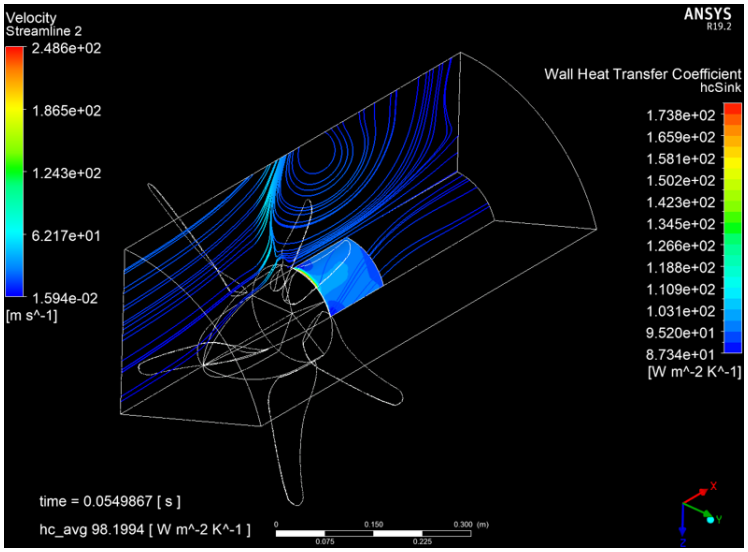

Fig. 10 ANSYS CFX external heat transfer characterization model showing the average heat transfer coefficient of 98.2 W/m^2K at an air velocity of

This model assumes a heat generation of 390 W at the motors location and the rotor spinning at 5400 RPM, while the aircraft is stopped on the runway. The model simulates the air stream curvature around the heatsink resulting from the rotating blades, corresponding to roughly 30 m/s . The average heatsink convection coefficient of 98.2 W/m^2K is applied as a boundary condition to a high fidelity COMSOL thermal model depicting each component.

B. COMSOL Component Thermal Modeling

A high fidelity model of thermally participating solids within the HLM was assembled in COMSOL. Heat source terms, obtained from the component loss buildup, were applied to the stator irons windings, magnets, bearings, and rotor hub. Table 6 shows the thermal conductivity and materials used for this analysis.

Table 6 Thermal conductivity properties of materials used for the thermal analysis of the HLM

Material	Thermal Conductivity @ 20 $^\circ C$ (W/m$^\circ C$)
2024-T3	120
Hiperco-50	20
Copper	400
Epoxy	1
Windings @59% fill	237.6 (Radial), 2.49 (Axial)
N48H Magnets	9

The thermal transport properties of the slot area is very sensitive to the copper fill factor. An area-weighted correlation was used to model the copper wire bundles [11], which can be see in Equation 6 for the radial thermal conductivity, and in Equation 7 for the axial thermal conductivity.

$$K_{radial} = \frac{k_e * k_c}{(1 - Cu_f) * k_c + Cu_f * k_e} \tag{6}$$

$$K_{axial} = Cu_f * k_c + (1 - Cu_f) * k_e \tag{7}$$

Where K_{radial} is the homogenized radial thermal conductivity, K_{axial} is the radial thermal conductivity, k_c is the copper thermal conductivity, k_e is the epoxy thermal conductivity, and Cu_f is the copper fill factor. The end windings

are then assumed to be homogenized, but anisotropic, requiring the coordinate system be continuous and correctly oriented for each segment.

Steady-state thermal power for each motor assembly component are applied as uniformly distributed heat fluxes across their respective bodies. Surface averaged heat transfer coefficients for each surface group were mapped from the CFX breakout model to their corresponding locations in the COMSOL assembly, assuming no thermal contact resistance. Based on this steady state thermal analysis, assuming no air flowing internally, at the combined worst case scenario, all temperatures remain below maximum allowable operational temperatures. Figure 11 displays the final losses from each component, the temperature output by the thermal analysis, and the maximum allowable temperature for each component.

Component	Losses (W)	Max Allowable Temp (°C)	Steady State Temp (°C)
Stator Windings	253.8	200	**128.65**
Stator Iron	117.6	N/A	**127.99**
Heatsink	N/A	N/A	**116.36**
Rotor Magnets	15	120	**89.97**
Rotor Iron	3.85	N/A	**78.10**
Fwd Bearing	24	100	**89.48**
Aft Bearing	29	100	**95.68**

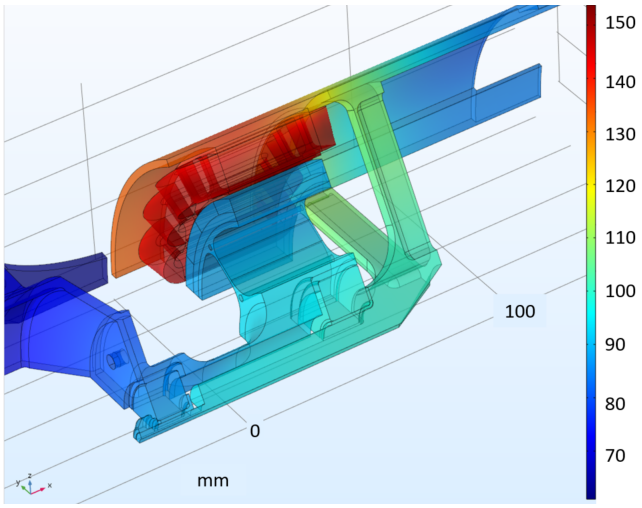

Fig. 11 Converged losses for each component with the final temperatures reached in the steady state analysis, compared to the maximum allowable temperature of each component, if applicable.

Now that the thermal behavior matches the initial steady state temperature design assumptions, this design is converged through the first four steps of Fig 4. iteration is then passed to the nacelle and support hardware step, and the rotordynamic design step simultaneously. The nacelle and support hardware step will be discussed in the next section.

VI. Hardware and Static Load Analysis

The nacelle hardware designed for the HLM consists of a heatsink and rotor hub, which was designed in parallel with the rotordynamic analysis. Analysis of the detailed support hardware such as the bearings, springs, fasteners, and bushings, all of which have also been designed and analyzed, are not included in this report. The hardware is required to support motor operation with regards to stress, thermal loading, and frequency management. Figure 12 depicts the nacelle and motor design, which includes the heatsink and some of the primary interior support structure, with the HLM installed. The heatsink in dark gray, and rotor hub in red are the only two parts of concern for this section.

The heatsink and rotor hub have gone through stress analysis assuming worst static loading cases for the X-57. The hardware has been analyzed for thermal considerations as well to ensure heat is properly distributed through the heatsink. The final geometry of the heatsink and additional hardware is passed to the rotordynamics analysis which will be discussed in the next section.

A. Static Stress Analysis

The heatsink and rotor hub were designed assuming the worst case load scenario. Table 13 shows all load cases, with the worst case highlighted in yellow. For the rotating rotor hub, 5,600 RPM and 24 Nm of torque was assumed about the axis of rotation due to the propeller reaction force. Body accelerations of 1.33 G span-wise and 3.4 G vertical accelerations are also taken into account. 414 N of thrust is applied in the axial direction while 119 N is applied in both the span-wise and vertical directions to account for asymmetric propeller effects seen at high angles of attack. To account for gyroscopic loads due to max sideslip and angle of attack, 29 Nm is applied about the span-wise direction,

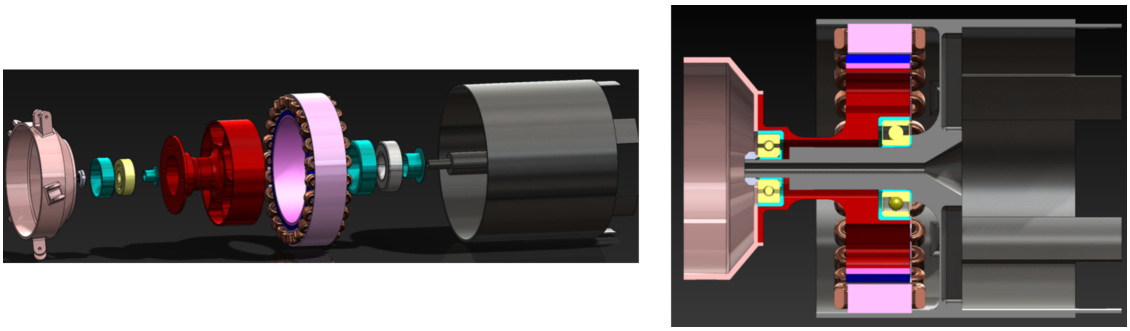

Fig. 12 Left: HLM assembly broken out with primary pieces displayed, of primary concern is the heatsink (dark gray), and the rotor hub (red). Right: HLM installed inside the heatsink.

while 44 Nm is applied about the vertical direction. For all loads previously described, excluding the inertial loads, the location of application is the propeller centroid.

After altering the thickness of the outer diameter of the heatsink, it was found the thickness was sensitive to heat distribution and dissipation. For this reason, thermal analysis required the geometry of the heatsink. This relation can be seen in Fig 4 as the hardware design is passed back into the thermal behavior step. Rotordynamics required the shape of the center shaft of the heatsink, the shape of which was largely driven by the frequency response. The rotor hub is largely driven by reducing mass and maintaining positive margin for the stress analysis.

Critical Load Case Summary For HL Motor & Nacelle										
Load Case	Inertial Limit Loads (applied at motor CG Location)			Propeller Limit Loads (applied at propeller)						Comments
	Nx (g)	Ny (g)	Nz (g)	Fx (N)	Fy (N)	Fz (N)	Mx (Nm)	My (Nm)	Mz (Nm)	
1	0.0	-1.33	-3.4	-414	-119	119	24	29	44	Inertial + Thrust + Torque + Gyroscopic Loads + P-factor + Imbalance
2	0.0	-1.33	2.0	-414	-119	119	24	29	44	
3	0.0	-1.33	-3.4	-414	-119	-119	24	-29	44	
4	0.0	-1.33	2.0	-414	-119	-119	24	-29	44	
5	0.0	-1.33	-3.4	-414	-119	119	-24	29	44	
6	0.0	-1.33	2.0	-414	-119	119	-24	29	44	
7	0.0	-1.33	-3.4	-414	-119	-119	-24	-29	44	
8	0.0	-1.33	2.0	-414	-119	-119	-24	-29	44	
9	-3.0	1.33	2.0	0	0	0	0	0	0	Ground Loads - not critical
10	0.0	0	0.0	-225	225	225	0	0	0	Ground Handling / Abuse Loads

Fig. 13 List of static loading scenarios the X-57 will encounter. Number 1 is the worst case scenario used for stress analyses.

The heatsink and rotor hub are constructed from 2024-T3 aluminum, per AMS-QQ-A-200/3, with an ultimate tensile strength of 54,000 psi in the long transverse (LT) direction and an ultimate shear strength of 33,000 psi in the long (L) direction. Due to an applied thermal load factor of 1.2, the ultimate tensile and shear strength of the aluminum is reduced to 49,800 psi and 30,433 psi respectively, which corresponds to 110 $^{\circ}C$ and 92% of the original strength values.

ANSYS Workbench was used to perform the finite element analysis (FEA) to obtain stress contours for the HLM hardware components. The maximum and minimum principal stresses are analyzed and ultimate factors of safety are used to ensure the stresses stay in the linear elastic stress-strain regime. The final design for the heatsink resulted in a maximum principle stress of 14,960 psi, which yields a positive margin of safety of 0.29, a factor of safety of 2.25, and a fitting factor of 1.15. Figure 14 shows the FEA analysis, due to the nature of the cantilevered shaft, the peak stress locations are near the base of shaft where the struts meet the shaft. The heatsink has a relatively large margin of safety because this piece was vibration constrained, and required additional material near the base of the shaft.

The rotor hub was analyzed for maximum loading and torque because this part will be rotating with the rotor at a maximum speed of 5,460 RPM. The rotor hub will be mounted to the rotor and does not require centrifugal force analysis; the electrical steel of the rotor provides the necessary rigidity. Figure 15 shows the maximum stress of 18,802 psi, which translates into a positive margin of safety of 0.04 with the same factors of safety used in the heatsink analysis .

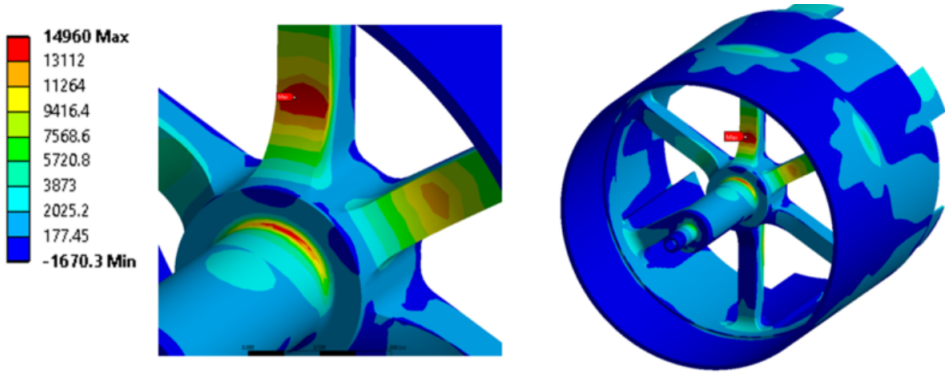

Fig. 14 Heatsink static stress analysis showing a maximum principle stress of 14,960 psi, resulting in a positive margin of safety of 0.29

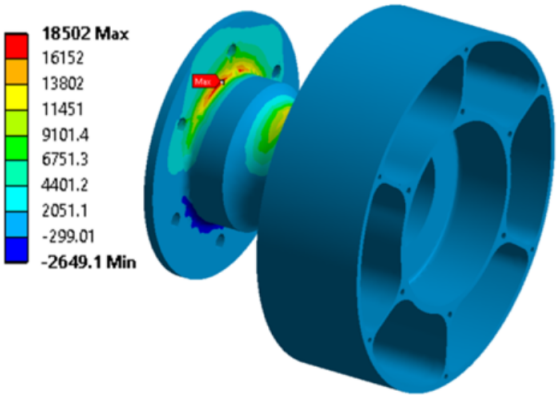

Fig. 15 Rotor hub stress analysis showing a maximum principle stress of 18,802 psi, resulting in a positive margin of safety of 0.04.

Not discussed here are the finer details concerning the bearing selection and preloading, stator potting details, or the mechanical construction of the motor. While this was all complete, it was considered out of the scope for this report but will detailed in follow on reporting. Please refer to Fig 24 in the appendix for the mechanical drawing of the rotor hub, and Fig 25 in the appendix for a mechanical drawing of the heatsink.

B. Air Gap Stack-up

If the rotor magnets should make contact with the inner diameter of the stator during operation, a catastrophic failure can occur. It is important to understand if the air gap between the magnets and the stator is sufficient at 1.0 *mm*. The air gap tolerance table should take into account all worst case hardware machining tolerances, at the worst case load displacement, and the worst case vibrational displacement from the rotor dynamics. This is done to ensure there will be no contact between the high-speed rotor and the stator inner diameter. Table 7 lists the air gap stack-up which shows there will be no contact between the rotor and stator, instead, an excess of 0.1088 mm of space will exist.

VII. Rotordynamic Performance

There are two basic rotordynamics requirements for the X-57 HLM. The first is that any rotordynamic resonance frequency needs to be at least twice the rotor speed of 5400 RPM, or 90 Hz. The second is that the motor needs to be able to handle a large unbalance at the propeller location. The requirement that rotordynamic resonance frequencies be at least twice the rotor speed means that there will be no critical speeds during operation; a critical speed is a rotor speed at which the rotor unbalance can excite a resonance mode. Thus any propeller unbalance should not result in large

Table 7 Air gap tolerance stack-up for the 1.0 mm air gap between the magnets and the stator inner diameter

Displacement Mechanism	Length (mm)
Rotor mode displacement	0.020
Heatsink static load displacement	0.287
Carbon fiber retainment wrap	0.381
Magnet tolerance	0.0508
Rotor tolerance	0.0762
Stator tolerance	0.0762
Total material in 1.0 mm air gap	0.8912

resonant displacements or bearing forces, since the response will be off-resonance.

Since the motor drives the propeller directly, it acts as a large mass at the end of the rotor shaft which results in an overhung rotor. This will drive down the frequency of the conical mode. In addition, it was decided to use a non-rotating inner stator shaft to also drive down the conical frequency since the stator will be more compliant. To keep the conical mode frequency above twice the rotor speed, the inner stator shaft and support structure were made as stiff as possible, with a larger bearing at the aft end of the shaft while keeping the mass as low as possible. Figure 16 shows the hardware designed to house the motor, and the motor installed within the hardware.

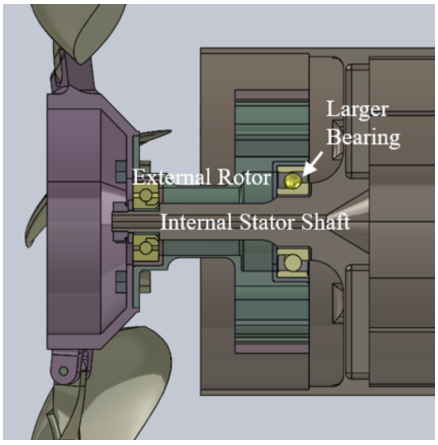

Fig. 16 Motor structure, showing the layout of the motor inside the X-57 nacelle with the propellers attached to the shaft (left side). The dark green portion is the External Rotor, labeled in the figure, is the rotating part.

A finite element analysis was performed on the motor/propeller/hardware structure. There is some coupling between the conical rotordynamic mode and the propeller blades. However, some information about the propeller blades was unknown, so they were modeled in two ways – as stiff blades, and then as more compliant blades, both with bonded connection to the hub. Figure 17 shows the conical mode frequency as a function of rotor speed, for the two different assumptions on the propeller blade properties and 18 shows the rotordynamic conical mode shape for the stiff propeller assumption.

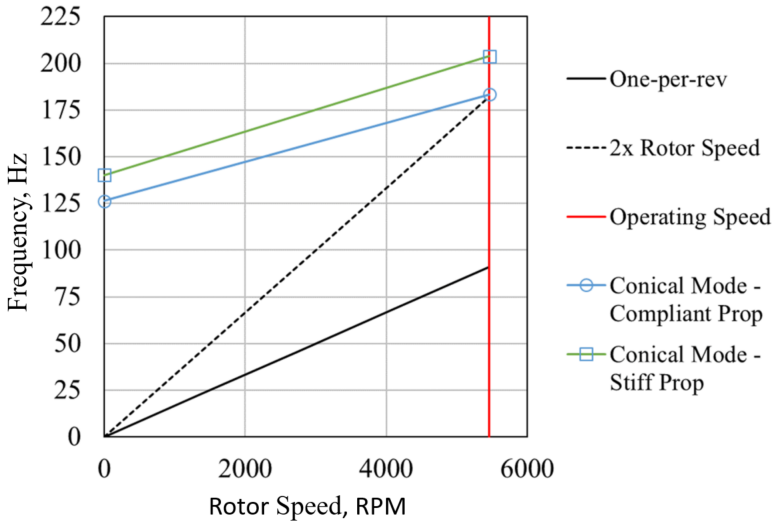

Fig. 17 Rotor resonance frequencies versus rotor mechanical frequency

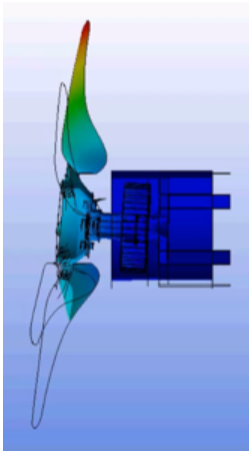

Fig. 18 Two dimensional representation of the conical mode shape

Figure 19 shows the results of all rotordynamic analysis completed for this structure. The worst case is the conical mode, as mentioned above, at a forward frequency of 183.4 Hz. This frequency still satisfies the requirement of being two times above HLM operational frequency of 90 Hz. Numbers in parenthesis represent a multiple of frequency separation, all of which satisfy the frequency requirements. The backwards whirl (BW) for each mode can be neglected here because the unbalanced mode does not excite this method. Therefore, the forward whirl (FW) is the only method for each mode to be fully analyzed.

Mode	Stiff Prop Blades		More Compliant Prop Blades	
	0 RPM	5460 RPM	0 RPM	5460 RPM
Conical	169.0	BW - 140.2 (N/A) FW - 203.9 (2.2)	152.3	BW - 126.4 (N/A) FW - 183.4 (2.0)
Torsion	190.5	523.9 (5.8)	158.5	338.0 (3.7)
Blade/Hub *	252.0	BW - 235.2 (N/A) FW - 270.6 (3.0)	178.0	BW - 173.2 (N/A) FW - 183.0 (2.0)
Blade Flap *	308.5	308.5 (3.4)	199.7	200.6 (2.2)

Fig. 19 Summary of all frequency modes analyzed, highlighting the difference between the stiff blade and the compliant blade models. The two bottom modes with asterisks (*) are notional at this time due to the propeller frequencies being unknown. The BW and FW annotations depict backwards and forwards whirl.

The unbalance response requirement is based on a propeller radial displacement of 0.005 inches at the operating speed of 5460 RPM. This results in maximum bearing loads of 7.4 lbs and 12.9 lbs for the smaller and larger bearings, respectively, well below the maximum allowable forces of the bearings. In addition, the radial displacement in the gap between the rotor and stator is less than 0.0025 inches, again much smaller than the gap. The propeller and rotor assembly should be balanced to a much smaller unbalance level, so it is unlikely that this large unbalance will occur in operation.

VIII. Conclusion and Future Work

The motor mass and power requirements proved to be difficult requirements to meet across the entire design spectrum. The mass requirement set forth by the X-57 project is 2.77 kg, and the HLM was able to meet and exceed this requirement by developing a motor with a mass of 2.34 kg. Table 8 lists the component weights for the HLM, and the supporting hardware. Note the total mass at the bottom of Table 8 references all materials summed up, the primary mass of concern is the total motor mass.

Table 8 Mass summary for the HLM and supporting hardware

Component	Mass (kg)
Stator	0.826
Rotor	0.099
Magnets	0.418
Windings	1.00
Total Motor Mass	**2.34**
Heatsink	0.677
Rotor hub	0.255
Hardware Total	**0.932**
Bearings and Bushings	0.267
Fasteners	0.075
Support Total	**0.342**
TOTAL MASS	**3.614**

The final HLM designed, satisfying all requirements and analysis can be seen in Fig 20, which is scheduled to be built and tested. All accompanying hardware has been designed and analyzed, and will be manufactured so that the HLM can be tested in an accurate setting to understand thermal and rotordynamic behavior while in operation. A bill of materials, seen in Table 9, is included with this design but does not include the supporting hardware manufacturing or

material costs.

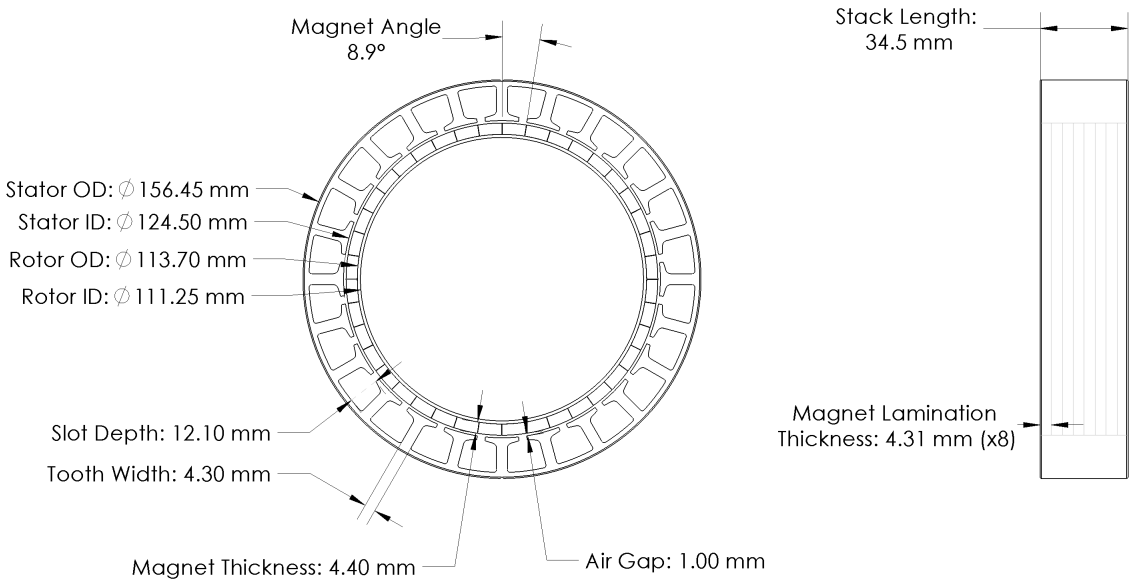

Fig. 20 Drawing and measurements of primary geometries on the prototype motor

Table 9 Bill of Materials for the HLM

Component	Material	Qty	Total Price
Laminated Stator	Hiperco-50	1 ea	$6,159
Laminated Rotor	Hiperco-50	1 ea	$4,664
Laminated Magnets	N48H Neodymium	1 set	$870
Slot Liner	Nomex 410 5 mil	1 sheet	$8.16
Aft Bearing	Steel	2 ea	$81.76
Fore Bearing	Steel	2 ea	$48.77
Litz Magnet Wire	Copper, Polyimide	500ft	$717
Potting Compound	Epoxy	2 pints	$430
Magnet Retainment	Carbon Fiber	1 ea	$1,300
Total Cost			**$14,278**

This paper provides an overview of the design process used to satisfy the X-57 flight requirements across several coupled disciplines. Different flight conditions are identified as the limiting design constraint for various aspects of motor performance. Low-level design codes were used for rapid preliminary design space exploration with final refinement performed using high-fidelity multiphysics finite-element analysis. Key active constraints are identified for each discipline and necessary convergence loops between electromagnetic, thermal, structural, and rotordynamics are identified. A final reference design is depicted meeting all vehicle requirements with a 16.8 % mass margin for the electric motor, a specific power of 5.64 kW/kg, and an efficiency of 96.6%. The intention of this work is to serve as an open reference baseline design for passively cooled aircraft electric motor performance and as a starting point for more detailed optimization. A series of offline and online tests will reveal the accuracy of work and analysis performed here, and is scheduled to occur once the motor is constructed. Offline tests are required to ensure proper safety concerning the dielectric strength and insulation is sufficient to support normal operating conditions. These tests include a winding electrical resistance test, a DC high potential test, a megohm and polarization index test, and

a surge test at a minimum. Future work and publications will detail manufacturing lessons learned, detailed design considerations, and the online/offline testing procedures and results.

Appendix

As a fully open design, further refinement by external parties is encouraged. Complete motor designs and drawings will be made available on `https://www.nasa.gov/aeroresearch/X-57/technical/index.html`

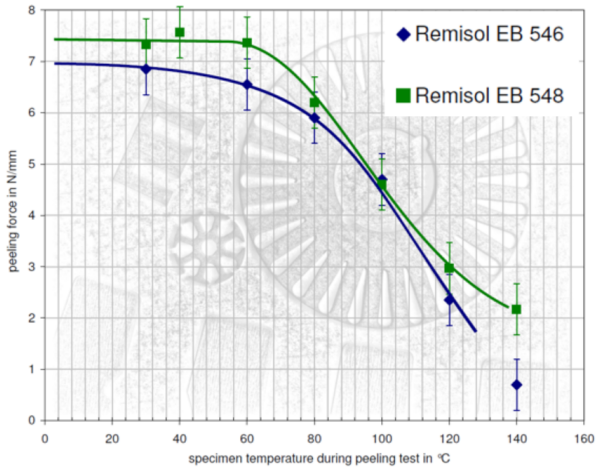

Fig. 21 Stator and rotor bonding varnish performance details

Table I. Typical Electrical Properties of DuPont™ Nomex® 410

Property	Nominal Thickness, mm (mil)											Test Method
	0.05 (2)	0.08 (3)	0.10 (4)	0.13 (5)	0.18 (7)	0.25 (10)	0.30 (12)	0.38 (15)	0.51 (20)	0.61 (24)	0.076 (30)	
Dielectric Strength AC Rapid rise, V/mil kV/mm	460 18	565 22	525 21	715 28	865 34	845 33	870 34	850 33	810 32	810 32	680 27	ASTM D149[1]
Full Wave Impulse, V/mil kV/mm	1000 39	1000 39	900 36	1400 55	1400 55	1600 63	N/A N/A	1400 55	1400 55	N/A N/A	1250 49	ASTM D3426
Dielectric Constant at 60 Hz	1.6	1.6	1.8	2.4	2.7	2.7	2.9	3.2	3.4	3.7	3.7	ASTM D150
Dissipation Factor at 60 Hz (x 10^{-3})	4	5	6	6	6	6	7	7	7	7	7	ASTM D150

1. Using 50-mm (2-in.) electrodes, rapid rise; corresponds with IEC 243-1 subclause 9.1, except for electrodes set-up of 50 mm (2 in.).

Fig. 22 Nomex 410 electrical properties

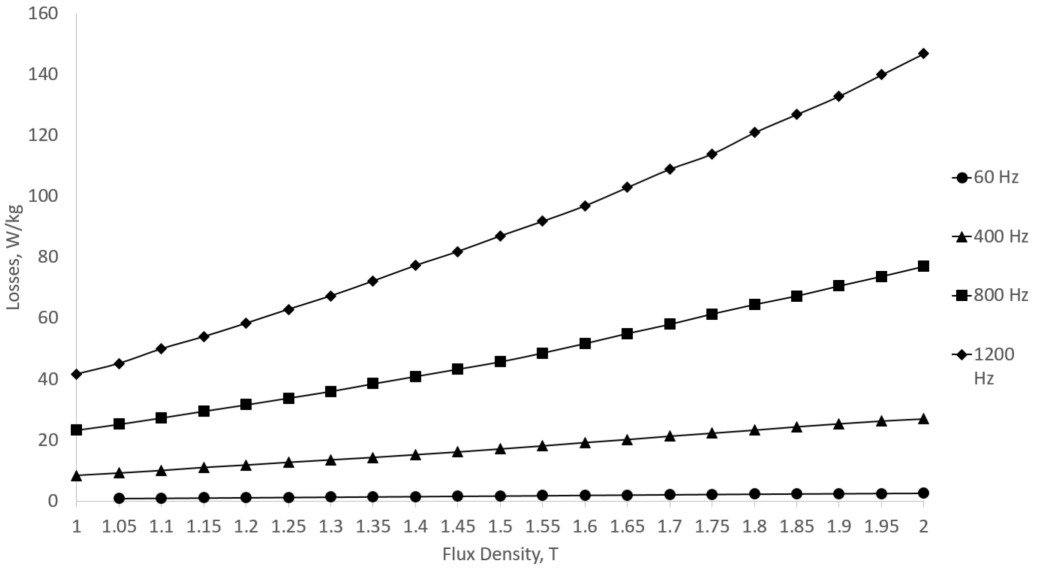

Fig. 23 Loss plots for various frequencies for Hiperco-50. Used to calculate empirical coefficients using the modified Steinmetz method.

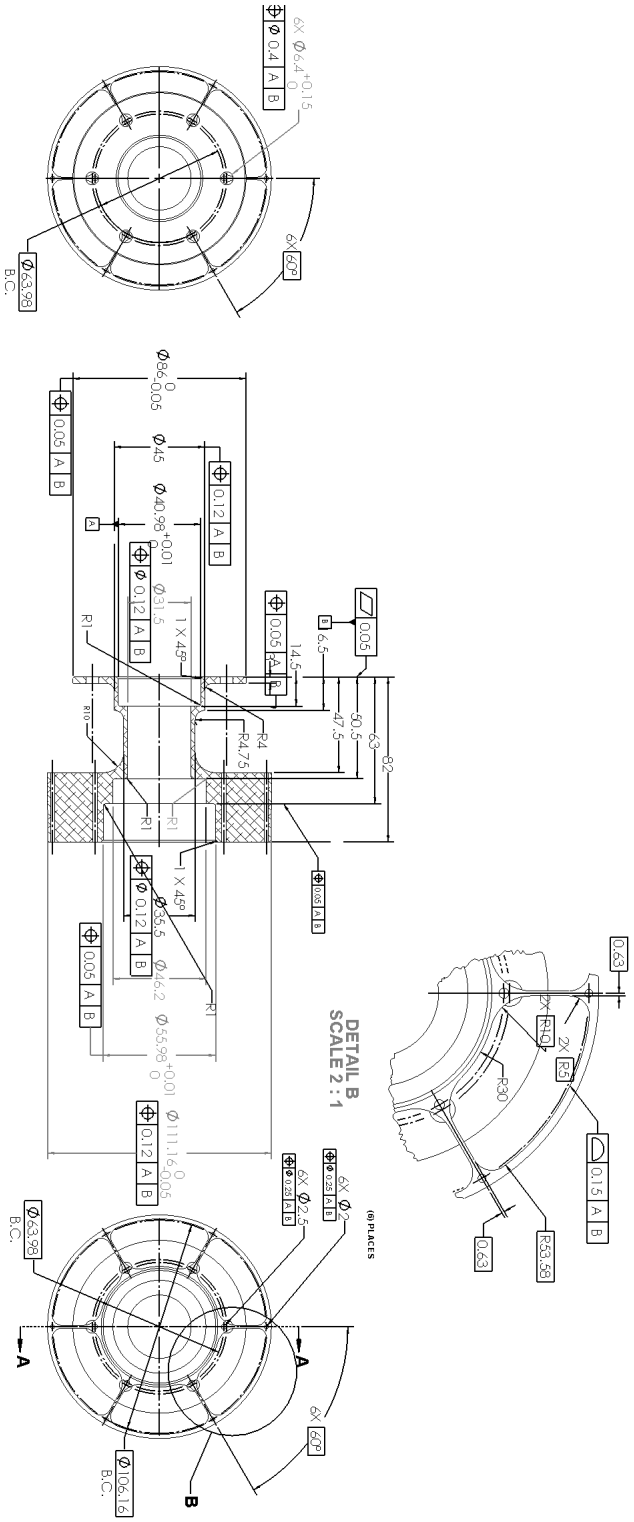

Fig. 24 Mechanical drawing for the rotor hub

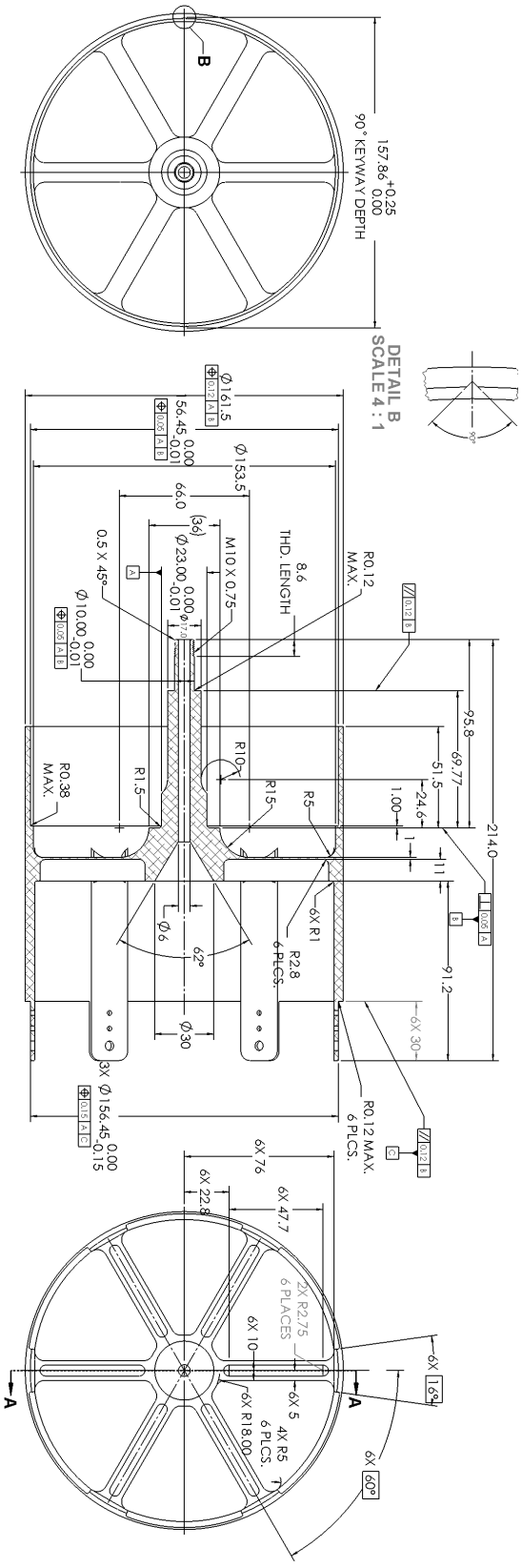

Fig. 25 Mechanical drawing for the heatsink

Acknowledgements

The authors would like to thank the X-57 team, Vantage Partners LLC, the Flight Demonstrations and Capabilities (FDC) Project and the Transformational Tools and Technologies (TTT) Project. Additional thanks to Ralph Jansen, Brian Motil, Peter Kascak, Thomas Cressman, and Justin Gray for serving on the design review board.

References

[1] Schnulo, L. S., Falck, R. D., Chin, J. C., Gray, J. S., Papathakis, K. V., Clarke, S., Reid, N., and Borer, N. K., "Development of a Multi-Phase Mission Planning Tool for NASA X-57 Maxwell," *Electric Aircraft Technology Symposium, AIAA*, 2018. URL `http://openmdao.org/pubs/x57_mpt_2018.pdf`.

[2] Harris, F., Borer, N. K., Redifer, M., Chin, J. C., Clarke, S., and M, Q., "SPEC-CEPT-004 X-57 High-Lift Motor Specification," *NASA, Armstrong Flight Research Center*, 2019.

[3] *ASTM A345 - 19: Standard Specification for Flat-Rolled Electrical Steels for Magnetic Applications*, American Society for Testing and Materials, International, West Conshohocken, PA, 2019.

[4] Ionel, D. M., Popescu, M., McGilp, M., Miller, T. J. E., Dellinger, S., and Heideman, R. J., "Computation of Core Losses in Electrical Machines Using Improved Models for Laminated Steel," *IEEE Transactions On Industry Applications*, Vol. 43, No. 6, 2007.

[5] Technologies, A. M., "Neodymium-Iron-Boron Magnet Grades; Summary Product List and Reference Guide," , 2019. URL `https://www.arnoldmagnetics.com/wp-content/uploads/2017/10/Catalog-151021.pdf`.

[6] Hanselman, D. C., *Brushless Permanent Magnet Motor Design*, Magna Physics Publishing, Lebanon, Ohio, 2006.

[7] Libert, F., and Soulard, J., *Investigation on pole-slot combinations for permanent-magnet machines with concentrated windings. International conference on electric machines*, Department of Electrical Machines and Power Electronics, Royal Institute of Technology, Stockholm, Sweden, 2004.

[8] Gieres, J. F., *Permanant Magnet Motor Technology, Designs and Applications*, Taylor and Francis Group, LLC, Boca Raton, Florida, 2010.

[9] *IEEE 95-2002 - IEEE Recommended Practice for Insulation Testing of AC Electric Machinery (2300 V and Above) With High Direct Voltage*, 2002.

[10] *ANSI/NEMA MW 1000-2016, American National Standard Magnet Wire*, National Electrical Manufacturers Association, Rosslyn, Virginia, 2016.

[11] Siesing, L., Reinap, A., and Anderson, M., "Thermal properties on high fill factor electrical windings: Infiltrated vs non infiltrated," 2014.